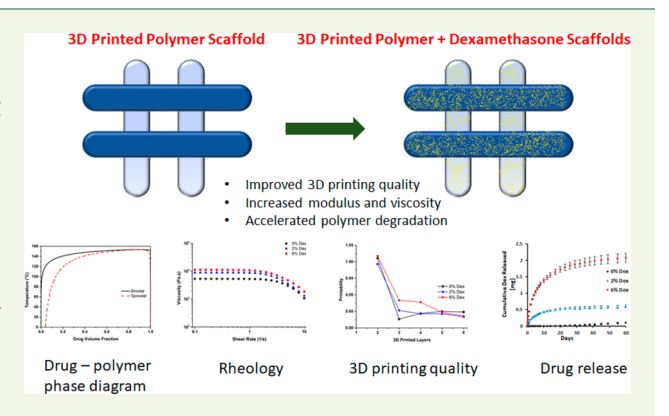


# Effect of Dexamethasone on Room Temperature Three-Dimensional Printing, Rheology, and Degradation of a Low Modulus Polyester for **Soft Tissue Engineering**

Tanmay Jain, †,‡ David Saylor,‡ Charlotte Piard,<sup>§</sup> Qianhui Liu,† Viraj Patel,<sup>§</sup> Rahul Kaushal, Ige-Won Choi, L,# John Fisher, Irada Isayeva,\*,‡ and Abraham Joy\*,†

Supporting Information

ABSTRACT: Three-dimensional (3D) printing has enabled benchtop fabrication of customized bioengineered constructs with intricate architectures. Various approaches are being explored to enable optimum integration of such constructs into the physiological environment including addition of bioactive fillers. In this work, we incorporated a corticosteroid drug, dexamethasone (Dex), in a low modulus polyester (SC5050) and examined the effect of Dex incorporation on solvent-, initiator-, and monomer-free pneumatic extrusion-based 3D printing of the polymer. Dex-SC5050 interactions were characterized by plotting thermodynamic binary phase diagrams based on the Flory-Huggins theory. The effect of Dex composition on the 3D printability of the SC5050 polyester was examined by rheological characterization and by image analysis of each layer of the 3D



printed scaffolds. The drug release and the degradation of the polymer from the 3D printed scaffolds was used to analyze the effect of Dex composition on the performance of the 3D printed scaffolds. We found that Dex was insoluble in SC5050 polyester at relevant 3D printing temperatures and the insoluble drug particles physically reinforced the polymer, increasing the viscosity and the shear modulus of the base polymer. In addition, the reinforcing effect improved the shape fidelity of the printed filaments and the overall quality of the scaffolds. The Dex particles demonstrated a two-phase release, with an initial burst release and a slower sustained release of drug under in vitro conditions. To investigate preliminary host response of the 3D printed SC5050 scaffolds for tissue engineering applications, the printed scaffolds were implanted subcutaneously in Sprague— Dawley rats for 6 weeks and examined for fibrous tissue formation, infiltration of cells, and vascularization into the pores of the scaffolds.

KEYWORDS: 3D printing, fidelity, low modulus polyesters, dexamethasone, drug delivery, phase diagram, degradation, rheology, tissue engineering

# ■ INTRODUCTION

Three-dimensional (3D) printing is being widely used for tissue engineering applications ranging from precise anatomical models for complex surgeries to bioengineered tissue constructs.1-6 Clinically implanted patient specific biomedical products like tracheal splints, sternum implants, and cranial and maxillofacial implants have demonstrated the potential of 3D printing for making complex constructs beyond the ability

of traditional fabrication methods. 5,7-9 The promise of 3D printing in tissue engineering lies in its ability to not only produce customized complex geometries to fit an irregular defect site but also to create a precise microarchitecture to

Received: August 14, 2018 Accepted: December 13, 2018 Published: December 13, 2018

Department of Polymer Science, The University of Akron, 170 University Avenue, Akron, Ohio 44325, United States

<sup>&</sup>lt;sup>‡</sup>Center for Devices and Radiological Health, Office of Science and Engineering Laboratories, Division of Biology, Chemistry and Materials Science, U.S. Food and Drug Administration, 10903 New Hampshire Avenue, Silver Spring, Maryland 20993, United

<sup>§</sup>The Fischell Department of Bioengineering, University of Maryland, College Park, Maryland 20742, United States

University of Maryland, Baltimore Campus, 620 W Lexington Street, Baltimore, Maryland 21201, United States

<sup>&</sup>lt;sup>1</sup>University of Maryland, College Park, Maryland 20742, United States

<sup>\*</sup>Department of Mechanical Engineering, The University of Akron, Auburn Science and Engineering Center, 244 Sumner Street, Akron, Ohio 44325, United States

Scheme 1. Synthesis Scheme for the SC5050 Polyesters

mimic native tissue complexity. <sup>1,3,5,10</sup> Optimum clinical outcomes may be achieved using 3D printed constructs that can mimic the structural architecture of the endogenous tissue and provide functional cues to benignly integrate into the physiological environment. <sup>1,5,11,12</sup>

However, most synthetic polymers such as polyethylene glycol (PEG), polylactic-*co*-glycolic acid (PLGA), and polycaprolactone (PCL)<sup>5,17-20</sup> used for 3D printing in the field of tissue engineering lack functionality to interact or elicit a favorable response from the host body.<sup>1,5</sup> On the other hand, although naturally derived polymers like gelatin, alginate, and collagen, have functional cues to induce cell attachment and proliferation, they suffer from batch-to-batch variability, scalability issues, and immunogenicity.<sup>1,5</sup> Therefore, therapeutic fillers like drugs, minerals, and biologics are often incorporated to impart biological activity in an implant.<sup>21</sup>

Therapeutic fillers are used ubiquitously to improve bioactivity and modify the mechanical properties of 3D printed implants. A variety of active pharmaceutical ingredients (APIs) such as steroidal anti-inflammatory drugs, acetaminophen, paclitaxel, ovancomycin, doloxacin, tetracycline, felodipine, folic acid, and others have been incorporated in 3D printed devices. However, the above studies have focused mainly on the physiological effects of the fillers but not enough attention has been given to studying the effect of incorporation of such therapeutic fillers on the 3D printability of the base polymer and the resultant quality of the 3D printed construct.

The effect of general fillers on the processing conditions of polymers is generally well-known. 34,35 Biologically inactive fillers like silicon-carbide have been shown to increase mechanical properties and improve 3D printability of the base polymer. 36 Fillers like metal particles have been reported to dramatically improve the quality of 3D printed constructs. 47 However, in the case of active ingredients like drugs, the polymer rheology, and therefore its printability, may change based on the specific drug—polymer interactions and the extent of drug solubility and miscibility in the polymer. 38,39

Although drug—polymer mixtures have been 3D printed for drug delivery applications, these systems are primarily fused deposition modeling (FDM) based and require high temperatures to be printed. The high temperature processing reportedly improves drug—polymer interactions leading to more homogeneous drug—polymer mixing. However, such high temperature may be unfeasible for printing temperature sensitive therapeutic fillers like drugs, growth factors, proteins, and other biologics. Therefore, it is of interest to investigate the relationship between drug—polymer interactions at room

temperature and the printability and 3D print quality of the drug loaded polymer matrix.

To investigate the effect of drug-polymer interactions on extrusion-based, room temperature, 3D printing of polymers, we chose a previously reported amorphous polyester (SC5050)<sup>49</sup> and a commonly used anti-inflammatory corticosteroid drug, dexamethasone (Dex), as the model drug. The SC5050 polyester is comprised of fatty acid side chains derived from soybean oil (S) and a photo-cross-linking group called coumarin (C). The polymer is made of an equimolar ratio of the two monomers, hence called SC5050, and can be 3D printed via extrusion based direct writing at room temperature without using any additives or solvents. Since it is a one component system that can be printed at room temperature conditions, it makes for an ideal candidate to examine the effect of Dex on its rheology and printability. Dex is a commonly used drug for modulating biological response to implants and in tissue engineering applications.

We used a widely reported method based on differential scanning calorimetry and the Flory–Huggins (F–H) solution theory to construct thermodynamic binary phase diagrams. The change in Gibbs free energy of mixing ( $\Delta G_{\rm mix}$ ) at ambient temperatures was determined by calculating the F–H interaction parameter ( $\chi$ ) for the Dex–SCS050 polyester system. Based on the free energy expression, the temperature–composition phase diagram was constructed.

Furthermore, we analyzed the effect of the composition of Dex on the shear rheology of SC5050 polyesters. To understand the effect of Dex on the print quality of the SC5050 polyester, the geometrical features such as line width and porosity of the 3D printed constructs made with various drug—polymer compositions were compared. A shape descriptor parameter, circularity, was used to evaluate the printability of the drug—polymer compositions. Moreover, since therapeutic fillers have been known to modify the degradation and resorption kinetics of a polymer matrix, <sup>17,57,58</sup> the effect of Dex composition on the drug release and degradation of the 3D printed SC5050 scaffolds was examined. Furthermore, as a preliminary assessment of biocompatibility, the 3D printed SC5050 scaffolds were implanted subcutaneously in Sprague—Dawley rats for 6 weeks.

## MATERIALS AND METHODS

**Materials.** All chemicals were used as received unless otherwise stated. *N,N'*-Diisopropylcarbodiimide (DIC, 99%) and 18-crown-6 (99%) were purchased from Oakwood Chemical. Soybean oil (SBO) was purchased from MP Biomedicals. Methyl 4-bromobutyrate (98%) was purchased from Chem-Impex. Adipic acid (99%) was purchased from Acros Organics. Diethanolamine (DEA, 99%) was purchased

from AMRESCO and lyophilized before use. 4-Methylumbelliferone (97%) and sodium methoxide (NaOCH3, 98%) were purchased from Alfa Aesar. 4-(Dimethylamino)pyridinium 4-toluenesulfonate (DPTS) was prepared according to literature methods. Reagent grade dimethylformamide (DMF) and methylene chloride (CH<sub>2</sub>Cl<sub>2</sub>) were purchased from Thermo Fisher Scientific and dried by distilling over anhydrous CaH2. Reagent grade tetrahydrofuran (THF), methanol (MeOH), ethyl acetate (EtOAc), acetone, and dimethyl sulfoxide (DMSO) were used as received from Thermo Fisher Scientific. Silica gel (40-63  $\mu$ m, 230  $\times$  400 mesh) for chromatography was purchased from Sorbent Technologies, Inc. Phosphate buffered saline solution (10x) was purchased from Thermo Fisher Scientific and diluted to 1× solution using HPLC grade water from Thermo Fisher. Dexamethasone (≥98%) was purchased from Sigma-Aldrich.

The monomers, N,N-bis(2-hydroxyethyl)-4-((4-methyl-2-oxo-2Hchromen-7-yl)-oxy)butanamide (C) and N,N-bis(2-hydroxyethyl)soybean amide (S) were synthesized as previously reported by our lab. 49 The polymer, SC5050, was synthesized by a polycondensation reaction of the (C) and (S) diols in equimolar ratio with adipic acid (Scheme 1).4

Drug-Polymer Mixing. The SC5050 polyester and Dex were mixed by dissolving in a cosolvent. SC5050 was dissolved in methylene chloride (CH2Cl2) at very dilute concentrations (<100 mg/mL). This concentration was chosen to ensure complete polymer solubilization and to enable uniform mixing with the drug. Since Dexamethasone (Dex) has poor solubility in most pure solvents, an equal part mixture of methylene chloride and acetone was used that was reported to improve Dex loading.<sup>59</sup> Dex was mixed in this solvent mixture at a concentration of 0.5 mg/mL. The SC5050 and Dex solutions were mixed in the required proportions to obtain desired compositions used in this study. The solvents from the drug-polymer solution mixture were removed quickly by a rotary evaporator. The mixture was further freeze-dried overnight on a high vacuum line to ensure all the solvent was removed. All the samples were freshly prepared before the experiments and stored in a -15 °C refrigerator overnight when not being used. Similar process of rapid drying followed by freeze-drying has been reported previously to achieve amorphous dispersions of a drug in a polymer.

Constructing Dex-SC5050 Phase Diagram. Recently a number of articles were published that reported the use of differential scanning calorimetry (DSC) in combination with the F-H theory to construct polymer/drug phase diagrams and to estimate drug—polymer miscibility.  $^{50-53,61-63}$  The melting point depression data of known drug-polymer compositions were used to calculate the temperature dependence of the F-H interaction parameter,  $\chi$ . The relationship of  $\chi$  with temperature combined with the F–H solution theory was used to estimate the change in the free energy of mixing  $(\Delta G_{\text{mix}})$  for the drug-polymer mixture, and construct a drugpolymer temperature-composition phase diagram. Drug solubility and miscibility at room temperature were predicted based on the constructed phase diagram. A detailed discussion on the theoretical considerations of plotting the phase diagram can be found in the Supporting Information (S.1).

Differential Scanning Calorimetry. DSC experiments were performed to determine the  $T_{\rm m}$  of the drug in the drug-polymer mixture. Drug-polymer mixtures with 25%, 35%, 45%, 55%, 65%, and 75% w/w Dex in SC5050 polyester (Mw 15.9 kDa, PDI 1.7) were prepared. A 3-5 mg portion of each sample was packed in a hermetic aluminum pan with a lid. At least three samples of each composition were used for the melting point depression experiments. The experiments were done in the modulated DSC mode with a scan rate of 3 °C/min, frequency of 60 s, and modulation temperature of  $\pm 1$  °C. The  $T_g$  of the samples was determined by using the standard DSC mode for which the samples were held at -80 °C and then ramped to 300 °C at 10 °C/min. All the DSC experiments were performed on the Q200 system (TA Instruments). The instrument was calibrated with sapphire and indium standards at the same ramp rate as in the actual experiment.

Rheology. All rheological experiments were performed using an AR-G2 rheometer (TA Instruments). An 8 mm parallel plate was used, with the gap between the two plates kept constant at 400  $\mu$ m  $\pm$ 10  $\mu$ m for all the analyzed samples. The Dex-SC5050 samples used for the printability and 3D print quality study were used for the rheology experiments. Each sample was allowed to relax until a steady normal force of close to 0 N (±0.05 N) was obtained before starting the experiment. Ten points per decade were recorded for each experiment. The percent strain sweeps were done at frequency 1 Hz and 25 °C. The steady state flow steps were done at a low 1% strain inside the linear viscoelastic region, 1 Hz frequency, and 25 °C. The temperature ramp was performed at 2 °C/min ramp rate, 1 Hz frequency, and 1% strain.

**3D Printing.** The EnvisionTEC 3D-Bioplotter was used for the drug-polymer printability and print quality experiments. The SC5050 polyester (Mw 25.2 kDa, PDI 2.1) and Dex-SC5050 mixtures with 2% and 6% w/w Dex were each printed as 90° cross-hatch patterned scaffolds where the printed layers are alternatively perpendicular to each other. 64 All the 3D printed scaffolds were at least six-layered with layer thickness of 180  $\mu$ m and dimensions of 8 mm  $\times$  8 mm. The distance between two consecutive parallel strands of the cross-hatch pattern, also referred to as "porosity", was maintained at 1 mm. The speed of the print head was maintained at 0.5 mm/s for all the experiments. The Nordson SmoothFlow tapered tips with inner diameter of 0.410 mm (22 gauge) were used for all the experiments. The dispensed polymer and drug-polymer mixture was cross-linked with a broadband UV (wavelength 320-550 nm) spot-curing lamp, Sunspot 2 (Uvitron). The lamp had a source intensity of 10.8 mW/ cm<sup>2</sup> at the tip, and the tip to sample distance was maintained at 3 cm. The polymer was photo-cross-linked for 60 s after printing each layer, and the final construct was further cross-linked postprinting from the top for 180 s.

The SC5050 polyesters with 0%, 2%, and 6% w/w Dex were printed at 30 °C, 48 °C, and 52 °C, respectively, with applied pressure of 2.7, 4.3, and 4.7 bar, respectively. Before printing, each Dex-SC5050 composition was allowed to equilibrate at their respective printing temperature in the print head for at least four hours to ensure the polymer was heated uniformly in the loaded syringe. Six 10layered scaffolds of size 8 mm × 8 mm were printed using the same SC5050 polyester without Dex for implantation in rats for the biocompatibility study.

Due to further unavailability of the aforementioned instrument, the scaffolds for the in vitro drug release and polymer degradation experiment were printed on a 3D printing setup assembled in-house. The setup is described in detail in our previous work.<sup>49</sup> Using the previously optimized 3D printing parameters, similar crosshatch patterned 10 layered scaffolds were fabricated. A new batch of SC5050 polyester with Mw 26.2 kDa and PDI 1.9 was used for making these scaffolds. The Omnicure 2000 mercury powered UV system (FullSpectrum) was used to photo-cross-link the SC5050 polyester. The lamp had a source intensity of 12W/cm<sup>2</sup>, and the tip to sample distance was 3 cm. At least four scaffolds were printed for each Dex-SC5050 composition. The 3D printed scaffolds had a mean mass of 40.8 mg  $\pm$  2.2 mg with a standard deviation of 8.9 mg.

Drug Release and Polymer Degradation. The 3D printed scaffolds (n = 3) of SC5050 polyester (Mw 26.2 kDa) incorporated with 0%, 2%, and 6% w/w Dex were submersed in 10 mL of 1× phosphate buffer solution (PBS) and kept on an incubator shaker (with rpm of 120) at 37 °C for 60 days. The pH of the media was monitored and maintained at pH 7.4 by completely replacing the solution with 10 mL of fresh PBS for each time point. One milliliter of each of the collected solutions was scanned for UV-vis absorption in a quartz cuvette at wavelengths 300-700 nm using UV-vis spectrophotometer (Agilent 8453).

To analyze the resulting absorbance spectra  $(\alpha)$  as a function of wavelength  $(\lambda)$ , we assumed that each spectra should comprise of four peaks, to reflect the total number of absorbing chemicals in the Dex-SC5050 system. Specifically, Dex has maximum absorption wavelength ( $\lambda^{max}$ ) of 242 nm in PBS, while the monomers used to make the SC5050 polyester have the following  $\lambda^{max}$  values: soybean

monomer (S) 203 nm; coumarin monomer (C) 249 nm; and adipic acid 203 nm. Due to the proximity of the individual peaks, significant overlap was observed. Thus, to specify the maximum absorbance intensity associated with each compound  $(\alpha_i^0)$ , it was necessary to deconvolute the broad absorption spectra (more information in the Supporting Information (S.2)).

The drug release was calculated based on the estimated absorption intensity, obtained from the deconvoluted spectra, at  $\lambda^{\max}$  of Dex (242 nm). The amount of Dex in the collected solution was calculated based on the first order relationship between absorption intensity and concentration obtained from the standard curve of Dex solution. The cumulative amount, and the percent of Dex released (relative to the amount of Dex in each scaffold) was then plotted against time. The amount of Dex in each scaffold was estimated based on the initial drug loading in the Dex–SC5050 mixture and the weight of each scaffold.

The collected solution from the Dex release study was also analyzed to estimate the amount of the SC5050 polyester degraded and released in the PBS buffer by using UV—vis spectroscopy (see Supporting Information (S.3)).

The fraction of the amount of SC5050 polyester released in solution to the amount of polymer in each scaffold was then plotted as percent polymer released against time. The amount of SC5050 polyester in the 3D printed scaffolds was calculated based on the weight and drug composition of each scaffold before degradation.

**Scanning Electron Microscopy.** SEM images of the cross-section of the Dex–SC5050 polyester 3D printed scaffolds, before and after the drug and polymer release experiment, were recorded on JEOL-JSM-7401F with operating voltage as 4 kV. The scaffolds were immersed in liquid nitrogen and cut with a stainless-steel razor. The scaffolds were mounted upright on a SEM stub using carbon tape with their freshly cut cross-section facing upward. Each sample was sputter coated with gold for 30 s prior to analysis.

In Vivo Evaluation. Sample Preparation. All the surfaces of the 3D printer were wiped down with ethanol and care was taken to ensure sterility of the 3D printed scaffolds. Six 10-layered, 90° cross-hatch scaffolds of size 8 mm × 8 mm were 3D printed with the SC5050 polyester (Mw 25.2 kDa, PDI 2.1) for implantation in rats for the biocompatibility study. The 3D printed scaffolds were sterilized by UV irradiation in a laminar flow hood for 30 min and sealed in a Petri dish with parafilm tape until implantation. Since the intensity of UV light used in this step was much lower than the intensity of UV irradiation used for cross-linking during 3D printing, the impact of UV irradiation on material properties is expected to be negligible.

Animal Implantation. The Institutional Animal Care and Use Committee of the University of Maryland approved the study, and all animals were treated in accordance with the Guide for the Care and Use of Laboratory Animals. The experiment was conducted in six male Sprague—Dawley rats. A small incision was made on the back of each animal, and the scaffold was implanted in the subdermal space. The animals were euthanized after 6 weeks, and the samples and surrounding tissue were explanted. Each explanted tissue sample was preserved in paraformaldehyde (4%) for histological analysis.

Histological Analysis. Explanted tissue samples were processed, embedded in paraffin, and sliced (15  $\mu$ m slides) by Histoserv, Inc. (Germantown, MD). For histological evaluation, sections were stained with Masson's Trichrome. Six images were taken per sample in defined zones (Figure 10B) and subsequently analyzed using ImageJ. To quantify collagen surface area (stained blue) and cell surface area (stained purple), first hues were adjusted using the function Adjust/Color Threshold to isolate either blues or purples. The pictures were then made binary (Process/Binary), and the black surface area was measured (see Figure S.9. in the SI). Cell or collagen surface area were obtained by subtracting the area occupied by the scaffolds fibers to the black surface area. The number of blood vessels in each picture from different sections were manually counted. Blood vessels were identified as tubular structure with dark purple rim, filled with erythrocytes (stain light purple/red). All samples were evaluated in triplicate.

#### RESULTS AND DISCUSSION

Estimating Dex-SC5050 Interaction. The extent of drug-polymer interaction in a physical mixture determines the miscibility of the drug in the polymer, and can impact physical stability of a drug during 3D printing and during its release. Thus, the miscibility/solubility limit of a drug in the polymer dictates the phase behavior of a drug in the mixture, which in turn affects its release characteristics and bioavailability. Soluble drugs may also have a plasticizing effect that lowers the polymer's viscosity and can affect the 3D printing parameters. On the other hand, insoluble drugs will act as filler and tend to increase the viscosity and modulus of the base polymer. Therefore, it is of interest to estimate drugpolymer interactions to determine optimum processing conditions and produce prints with consistent performance.

Based on the Flory—Huggins solution theory, we computed the temperature—composition phase diagram for the Dex—SC5050 system, which is shown in Figure 1. The binodal curve

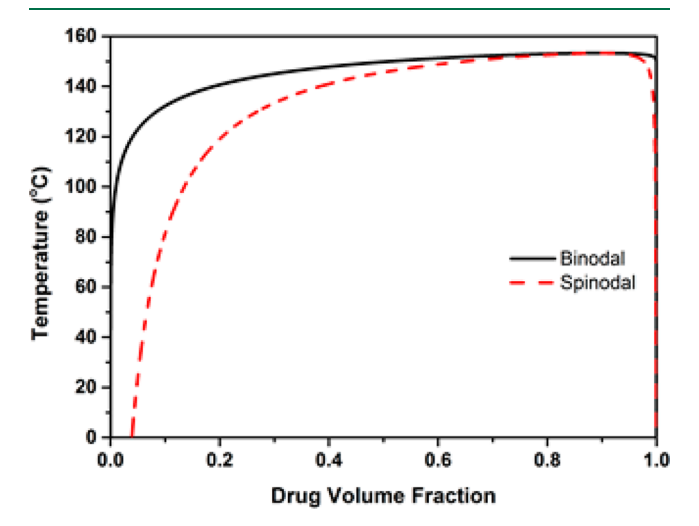


**Figure 1.** Binary phase diagram constructed based on Flory—Huggins theory using the melting point depression data for Dex in SC5050 polyester.

is the phase boundary which, at drug compositions below the critical point, represents the maximum solubility of Dex in the SC5050 polyester. Above this curve, the Dex–SC5050 system is stable as an amorphous mixture. The spinodal curve represents the miscibility boundary for the drug–polymer system. The drug–polymer system is unstable with respect to phase separation in the region below the spinodal curve. The region in between the spinodal and the solubility curves is the metastable region where the drug–polymer system can exist as a mixture, but sufficiently large composition fluctuations will lead to phase-separation by nucleation and growth. According to the plotted phase diagram, Dex is sparingly soluble (2  $\times$  10<sup>-5</sup> – 2  $\times$  10<sup>-4</sup>% w/w in the range of 25–50 °C) in the SC5050 polyesters and miscible at compositions below 5–6.5% w/w in the temperature range 25–50 °C used for 3D printing.

However, other than the thermodynamic barriers, phase separation (and recrystallization) of the drug is a complex process dependent on various factors like storage conditions (humidity, temperature), and other kinetic factors like  $T_{\rm g}$  of the polymer. At temperatures below the polymer  $T_{\rm g}$ , the glassy polymer structure limits drug mobility and hinders further

**ACS Biomaterials Science & Engineering** 

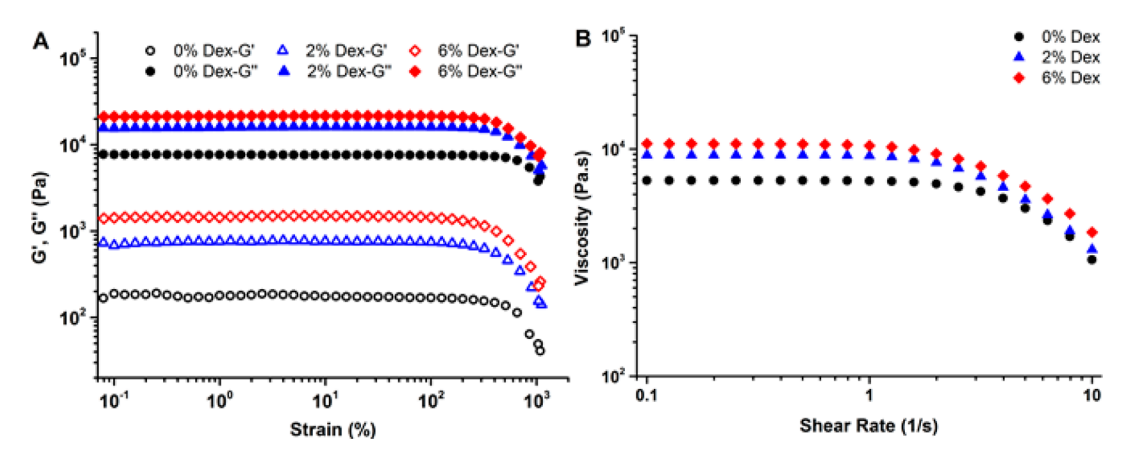


Figure 2. (A) Storage (G') and loss modulus (G'') vs percent strain sweep performed at 1 Hz frequency and (B) steady state viscosity vs shear rate, recorded at 25 °C for the various Dex-SC5050 compositions.

phase separation and recrystallization. However, at storage temperatures above  $T_{\rm g}$ , the higher molecular mobility enables phase separation to progress much more rapidly. Although the physical properties of the polymer like high viscosity and modulus may hinder the drug mobility in the polymer, the propensity for recrystallization at temperatures higher than  $T_{\rm g}$  is known to be remarkably greater due to the global mobility of the system. In the present case, SC5050 polyesters have a very low  $T_{\rm g}$  of about  $-30~{\rm ^{\circ}C}$  which is unaffected by the presence of the Dex at all studied compositions. Therefore, the SC5050 polymer likely offers no significant kinetic barriers to phase separation and recrystallization of the drug.

**Rheology.** For extrusion-based 3D printing, a material should be able to undergo shear thinning behavior in order to be extruded from a narrow nozzle. This non-Newtonian behavior causes a decrease in the material's viscosity in response to the high shear rates that are present in the nozzle, thus allowing the material to flow through the nozzle. Upon deposition, the shear rate decreases and the viscosity should sufficiently increase to be able to retain the printed shape and support overhang structures. Therefore, the 3D printability of polymers and drug—polymer mixtures is highly dependent on the rheological properties of these systems.<sup>67</sup>

The drug-polymer interaction based on the physical and chemical nature of the drug and the drug-polymer composition may affect the rheology and, therefore, the 3D printability of such systems. Many soluble drug molecules have been shown to act as a plasticizer and lower the viscosity of the base polymer. 38,67-69 On the other hand, if the drug is not soluble in the polymer, it will form a solid dispersion, and the drug particles can be considered to behave as reinforcing filler particles in the polymer. 66,67 The effect of various compositions of Dex on the SC5050 polyester rheology is shown in Figure 2. Oscillatory percent strain sweep measurements were performed on the SC5050 polyester with 0%, 2%, and 6% w/w Dex as shown in Figure 2A. The response of the polymer to the applied percent strain is recorded in terms of storage modulus G', which represents the elastic component, and loss modulus G'', which represents the viscous component of the material. G'' higher than G' for the SC5050 polyester with or without Dex indicates the predominantly viscous nature of the drug-polymer mixtures which enables it to flow and be 3D printed at low temperatures. However, the presence of Dex, even at such low concentrations, increases the G' and G'' of the SC5050 polyester. Moreover, the critical strain, at which

the material modulus starts decreasing, also starts to decrease with increasing Dex concentration. This drop in critical strain can most likely be attributed to the breakdown of the drug aggregates during the strain sweep. Therefore, the insoluble Dex particles likely form aggregates in the SC5050 polyester at all studied compositions.

The effect of Dex on the steady state flow behavior of the SC5050 polyester is shown in Figure 2B. The presence of Dex leads to an increase in zero-shear viscosity (viscosity at nearrest conditions), whereas the difference in viscosity for the SC5050 polyester and the Dex–SC5050 polyester mixtures decreases at high shear rates. Similar observations have been made for polymers filled with insoluble, inorganic fillers like carbon black, <sup>71</sup> talc, <sup>72</sup> and titanium dioxide. <sup>73</sup>

The SC5050 polyester shows shear thinning behavior where its viscosity reduces from 5.2 kPa.s at low shear rates to 1 kPa.s at high shear rates ( $\sim 10~\text{s}^{-1}$ ) typically experienced during 3D printing. <sup>67,74</sup> In case of Dex–SC5050 mixtures, the viscosity of 2% w/w and 6% w/w Dex in SC5050 polyester reduces from 8.8 kPa.s and 11.1 kPa.s at low shear rates to 1.3 kPa.s and 1.8 kPa.s at high shear rates ( $\sim 10~\text{s}^{-1}$ ), respectively. Clearly, the presence of Dex leads to more shear thinning of the SC5050 polyester. Moreover, the critical shear rate at which the viscosity starts decreasing reduces with increasing Dex composition (Figure 2B).

The high shear thinning behavior enables the drug—polymer mixture to be extruded through small nozzles without requiring deleteriously high printing pressures. Moreover, the increased shear thinning of the Dex—SC5050 polyester can be expected to improve the 3D printability of the mixture by reducing melt flow instabilities. Furthermore, the relatively higher storage modulus and zero-shear viscosity of the Dex—SC5050 polyester mixture at low shear rates can help maintain fidelity of the printed filamentary shape. He without the printed filamentary shape.

**3D Printing.** To understand the effect of Dex on the 3D printability of the SC5050 polyester, we first optimized the 3D printing conditions for the SC5050 polyester and then analyzed the effect of Dex on the 3D printing conditions. Moreover, to understand the effect of Dex on the quality of the 3D printed construct, the matrix dimensions and overall shape of the 3D printed scaffolds made with the SC5050 polyester were compared to those made with the Dex—SC5050 polyester mixtures.

The printability of the SC5050 polyesters was demonstrated in our earlier work.<sup>49</sup> The SC5050 polyesters with  $M_{\rm w}$  less than

80 kDa are predominantly viscous at room temperature. However, SC5050 polyesters with  $M_{\rm w}$  higher than 50 kDa were too viscous to be extruded and required high pressures beyond the instrument's capability. On the other hand, SC5050 polyesters with very low  $M_{\rm w}$  (<10 kDa) could not retain the printed shape when deposited. The SC5050 polyesters with  $M_{\rm w}$  in the range of 20–40 kDa were found to be ideal for printing and achieving optimum quality of the 3D printed constructs. Therefore, SC5050 polyester with  $M_{\rm w}$  of 25.2 kDa was selected for all the 3D print quality experiments. To analyze the effect of Dex on the printability of the polymer, SC5050 polyester mixed with 0%, 2%, and 6% w/w Dex was prepared to be 3D printed.

We hypothesize that by using equal volume of material in each 3D printed scaffold, and keeping the 3D printing parameters, such as printing speed, flow rate, layer thickness, tip inner diameter, matrix dimensions, and number of layers the same, any observed changes in the overall shape of the 3D printed construct may be attributed to the effect of Dex on the 3D printability of the SC5050 polyester. To achieve equal volume of material in the 3D printed scaffolds, the 3D printing temperature and pressure was adjusted for each Dex-SC5050 composition. Since the volume of the extruded material could not be calculated directly without expending a lot of material, the mass of the extruded material was determined instead. Each Dex-SC5050 polyester mixture was extruded for a fixed time at various pressures and its weight recorded. We assume that the low drug compositions used in this case (2% and 6% w/w) do not significantly affect the density of the Dex-SC5050 polyester mixture. Therefore, the 3D printing pressure for each Dex-SC5050 polyester mixture was selected by matching the weight of the extrudate to the weight of the SC5050 polyester extruded for the same time.

The SC5050 polyester with 0%, 2%, and 6% w/w Dex were printed at 30 °C, 48 °C, and 52 °C, respectively, with applied pressure of 2.7, 4.3, and 4.7 bar, respectively. Ideally, all the Dex—SC5050 polyester mixtures should be printed at the same temperature. The change in temperature can affect the drug—polymer interactions and, therefore, the drug miscibility and solubility in the polymer. However, to achieve the same flow rate as the SC5050 polyester at 30 °C, the drug loaded polymer required high pressures beyond the instrument's capability. Therefore, the temperature had to be increased to achieve similar flow rates for the drug loaded polymer.

We note that the 3D printing temperature could not be decided by directly matching the complex viscosity of the various compositions. The complex viscosity of the SC5050 polyester at 30 °C is 2.7 kPa·s. The SC5050 polyester with 2%, and 6% w/w Dex showed similar complex viscosity at 31.5 and 34 °C, respectively (Figure 3). However, we observed that much higher temperatures were required to extrude the 2% and 6% w/w Dex loaded SC5050 polyester. This may be because the complex viscosity is calculated by applying an oscillatory shear force, whereas during printing the drugpolymer mixture experiences both shear and extensional forces.

Using the aforementioned printing conditions, and keeping the printing parameters such as the printing speed, layer thickness, and tip inner diameter constant at 0.5 mm/s, 180  $\mu$ m, and 410  $\mu$ m, respectively, six-layered SC5050 scaffolds with and without Dex were printed. The 3D printed scaffolds were 8 mm  $\times$  8 mm with a crosshatch infill pattern. The alternating layers were printed at 90° to the initial direction of printing of the previous layer. Six layers were printed for each

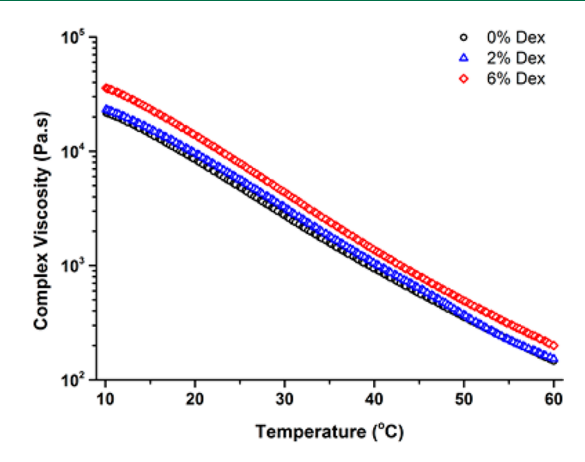


**Figure 3.** Complex viscosity vs temperature sweep performed at 1% strain and 1 Hz frequency with a temperature ramp rate of 2 °C/min.

scaffold of the Dex–SC5050 polyester compositions followed by cross-linking of each layer for 60 s. Figure 4 shows photographs of each layer captured by the in-built EnvisionTEC Bioplotter camera after each layer was printed and cross-linked.

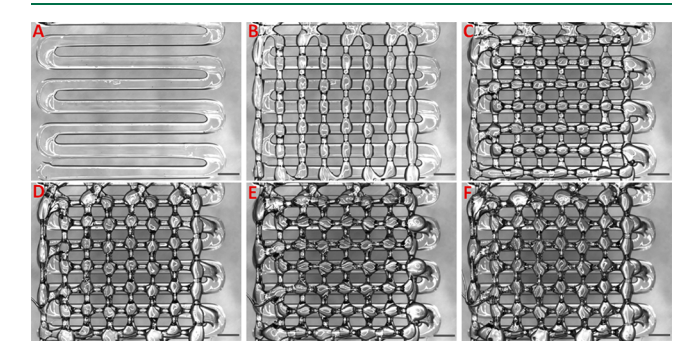


**Figure 4.** (A) First, (B) second, (C) third, (D) fourth, (E) fifth, and (F) sixth layer of the SC5050 polyester 3D printed scaffold (8 mm  $\times$  8 mm) (inset scale bar = 1 mm).

To understand the effect of Dex on the 3D print quality of the SC5050 polyester, we analyzed the dimensions of each of the first six 3D printed layers (Figure 4). The distance between two consecutive parallel lines of the cross-hatch pattern in the same layer, also commonly referred to as "porosity", was kept at 1 mm for all the 3D printed scaffolds. Ideally, the line width should stay constant for all the printed layers as shown in Figure 5A. However, we observed that the filament width of the first printed layer for all the Dex-SC5050 compositions is consistently higher than all the subsequent layers. This is likely due to the nature of the underlying surface. The first layer is printed on a glass substrate whereas the rest of the layers are printed on the previously deposited and cross-linked polymer layers. Moreover, the filament width in the first layer affects the dimensions of the second layer, which in turn affects the dimensions of the third layer. Interestingly, we observed that the layers beyond the third layer were not significantly affected and have similar dimensions.

Furthermore, we observed increased line thickness at the lattice intersections (also called nodes), compared to the line width of the bridge between two intersections, for the second layer and all the subsequent layers of the 3D printed scaffolds as shown in Figure 5B and C. At the intersection, the polymer

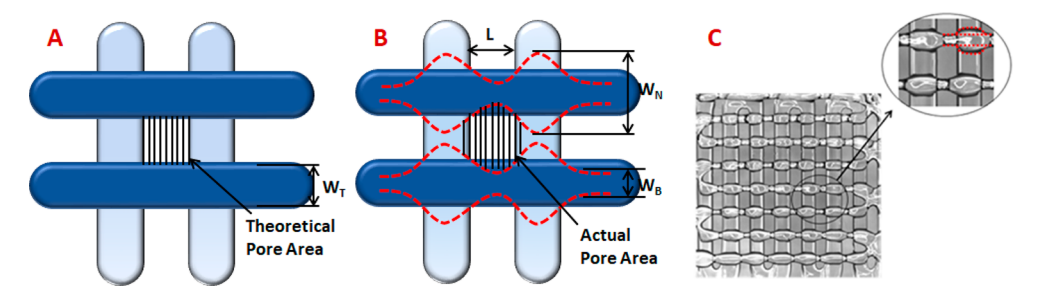


Figure 5. Schematic illustration of the (A) theoretical lattice and the (B) actual printed lattice. (C) Picture of the actual two-layered, 3D printed lattice of the SC5050 polyester. (inset) Zoomed in view of the area formed between two groups of adjacent straight lines.

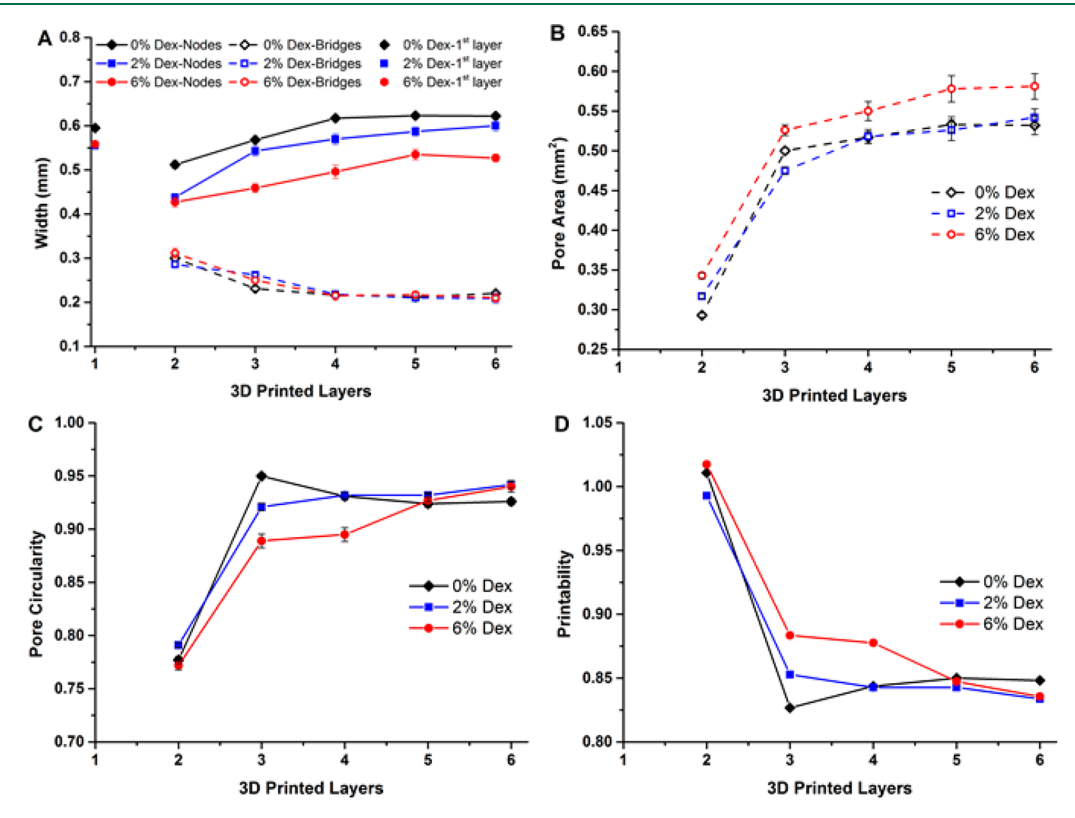


Figure 6. (A) Line width at intersection  $(W_N)$  and at the bridge  $(W_B)$ . (B) Actual area of the pores formed in between the crosshatch lattice. (C) Circularity of the pores. (D) Printability of the first six layers of the crosshatch lattice, for the SC5050 polyester mixed with 0%, 2%, and 6% w/w Dex. The error bars are smaller than the symbols.

melt diffuses and spreads along the surface of the previous layer leading to increased filament thickness. The layer being printed on remains largely unaffected since it is already cross-linked before the next layer is deposited. We call the line width at the intersection or width of the node, as  $W_{\rm N}$ , and the line width of the bridge between two intersections is labeled  $W_{\rm B}$  (Figure 5B).

Figure 7A shows the calculated  $W_{\rm N}$  and  $W_{\rm B}$  for the first six layers of each Dex–SC5050 composition. The difference between  $W_{\rm N}$  and  $W_{\rm B}$  increases from the second and third printed layer, and it remains nearly constant for the subsequent layers. The second layer, which is printed at 90° to the first layer, "sees" more of the first layer due to the higher line width of the first layer which leads to less spreading in the radial direction. Note that the length of the bridge (L), which is the distance between the two lines of the previous layer  $(L=1-W_{\rm N})'$ , where  $W_{\rm N}$  is the width at the node of the previous layer), is relatively less for the second layer. However, the length of the bridge is relatively higher for the third layer than the

second layer, which leads to more material being deposited at the intersection and thus higher  $W_{\rm N}$  and lower  $W_{\rm B}$ . The length of the bridge becomes nearly consistent after the third layer, and therefore, there is minimal change in  $W_{\rm N}$  and  $W_{\rm B}$  for the subsequent layers.

Moreover, the  $W_{\rm N}$  for each layer is relatively smaller for the drug loaded polymer than the polymer without any drug which suggests less spreading of the drug loaded polymer at the lattice intersection. This can be explained by the higher zero-shear viscosity of the Dex loaded SC5050 polyesters as seen in Figure 2B. We hypothesized that because the zero-shear viscosity of the drug/polymer mixture increases, the resistance to flow of the drug/polymer mixture increases, and the polymer spreads less before it is permanently set by photocross-linking. Furthermore,  $W_{\rm B}$  remains similar for all the Dex–SC5050 compositions for each layer.  $W_{\rm B}$  is unaffected by the presence of the drug in polymer because there is no contact with the previous layer, and therefore, no spreading of the overhanging filament in between two intersection points. Since

the flow rate was matched for all the Dex-SC5050 compositions, the amount of material deposited across the bridge is similar, and therefore,  $W_{\rm B}$  is similar for all the Dex-SC5050 compositions printed here.

The spreading of the polymer at the intersection also affects the area and the shape of the pores formed by the crosshatch pattern. The actual area of the pores was measured by tracing its outline in ImageJ software. Figure 6B shows the actual area of the pore  $(A_{pore})$  formed by each layer of the 3D printed lattice for the various Dex-SC5050 compositions. The area for each drug-polymer composition increases initially and becomes nearly constant beyond the fourth layer.  $A_{pore}$  is the lowest for the second layer because of the higher thickness of the first layer which leads to smaller pore area. Since the  $W_{\rm B}$ reduces with increasing layers, the pores become larger and the  $A_{\text{pore}}$  increases. Once  $W_{\text{B}}$  becomes constant, the  $A_{\text{pore}}$  also does not change after the fourth layer. Moreover, we observed that the  $A_{\text{pore}}$  of the drug loaded scaffolds is larger than the scaffolds without the drug for all layers. This is because the polymer spreads relatively less at the intersection in case of the drug loaded polymer, which leads to sharper corners and higher

 $A_{\text{pore}}$ .

Theoretically, the shape of the pores in a 90° crosshatch printed pattern is expected to be rectangular (Figure 5A). However, this area in the actual 3D printed lattice constructs appears to be irregular with curved corners (Figure 5B) formed due to the radial diffusion of the freshly printed polymer layer at the intersection. This shape of the actual pore area can be used to quantify the quality of the 3D printed lattice. Circularity (Cr) of an enclosed area is defined as following,

$$Cr = 4\pi \frac{[area]}{[perimeter]^2}$$

Cr = 1 defines a perfect circle. The closer the value of Cr is to 1, the closer the shape is to a circle. The Cr value of a square is  $\pi/4$ . Recently, Sun et al. 75 suggested defining the printability (Pr) of a 3D printed square lattice as

$$Pr = \frac{\pi}{4} \frac{1}{Cr}$$

For a perfect lattice (Figure 6A), the area formed between the interconnected printed lines would be square shaped with Pr =

Figure 6C shows the average circularity of the pores in each layer of the 3D printed lattice for the various Dex-SC5050 compositions. The pores in the second layer are square shaped, whereas the pores become more circular for the subsequent layers. This phenomenon can also be seen in the Pr values shown in Figure 6D. The Pr value is almost 1 for the second layer for all the Dex-SC5050 compositions, which suggests the pores are almost perfectly square. However, the Pr values reduce for the subsequent layers and approach 0.78, which is the Pr value for a perfect circle. Figure 7 shows the pictures of the six-layered Dex-SC5050 3D printed scaffolds. The scaffolds can be seen to change from translucent (Figure 7A) to opaque (Figure 7C) due to presence of immiscible Dex particles.

Drug Release. Figure 8A and B shows the rate of Dex released from the 3D printed scaffolds at each time point over 8 weeks. An initial burst release of Dex is observed over the first few days for the Dex loaded SC5050 scaffolds with a gradual decrease in the amount of released Dex over the

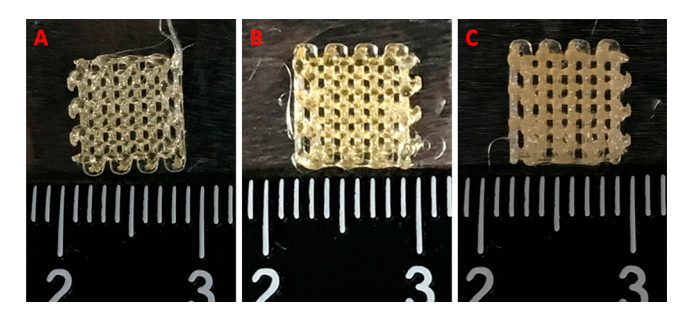


Figure 7. SC5050 polyester six-layered, 8 mm × 8 mm, 3D printed scaffolds with (A) 0%, (B) 2%, and (C) 6% w/w Dex. The scale is 1

remaining period. The rates of release of Dex during the first  $\boldsymbol{3}$ days are 82.5 and 288.3  $\mu$ g/day for the 2% and 6% w/w Dex in SC5050 scaffolds, respectively. The release rates then slow down to 20.1 and 70.4  $\mu$ g/day for 2% and 6% w/w Dex-SC5050 scaffolds, respectively, over the next 7 days. And during the last 3 weeks of the experiment, the drug release rates are 1.7 and 6.7  $\mu$ g/day for the 2% and 6% w/w Dex-SC5050 scaffolds, respectively (Figure S.6 in the Supporting Information).

Figure 8A shows the cumulative amount of Dex released from the 3D printed scaffolds over 8 weeks. As expected, the 6% w/w Dex in SC5050 scaffolds cumulatively release more drug than the scaffolds with 2% w/w Dex. Figure 9B shows the cumulative percent of Dex released from the 3D printed scaffolds. A biphasic release profile can be observed with an initial burst release phase, followed by a slow release phase. More than 50% of the loaded Dex is released in the first 10 days. Interestingly, the percent amount of loaded drug released during the burst phase is similar for the 2% w/w and 6% w/w Dex in SC5050 scaffolds (Figure 8B). Since the solution volume of PBS was relatively high (10 mL) and replaced frequently during the early stages of the experiment, drug saturation in the release medium was unlikely. Moreover, the amount of Dex released at any day was at least 1 order of magnitude below the solubility limit of Dex in water at 25 °C, and the drug concentration in each collected sample was within the concentration range of the standard calibration curve of Dex in PBS.

The burst release is attributed to the rapid release of surface connected drug-rich regions. 76,77 A number of causes for the burst release of drug from polymer matrices have been suggested, including the polymer matrix dimensions, hydrophobicity of the polymer and the drug, the polymer  $M_{\rm w}$ , drying processes, heterogeneous polymer matrices and defects, and the diffusion and migration of drugs toward the surface during fabrication or storage. 76 In case of the Dex-SC5050 scaffolds, the burst release could be explained by a combination of factors, such as the presence of surface connected drug rich domains, high scaffold porosity, polymer hydrophobicity, low polymer  $T_g$ , weak drug-polymer interactions, and the solubility of the drug in polymer relative to solubility of the drug in the aqueous buffer.

Since Dex is insoluble in the SC5050 polyester at ambient temperatures, the drug molecules phase separate from the polymer matrix. The low  $T_{\rm g}$  and amorphous nature of the SC5050 polyester promotes higher drug molecular mobility and migration of Dex toward the scaffold surface. 78 Moreover, the presence of water during the release stage may also reduce the  $T_{\rm g}$  of the polymer due to its plasticizing ability and

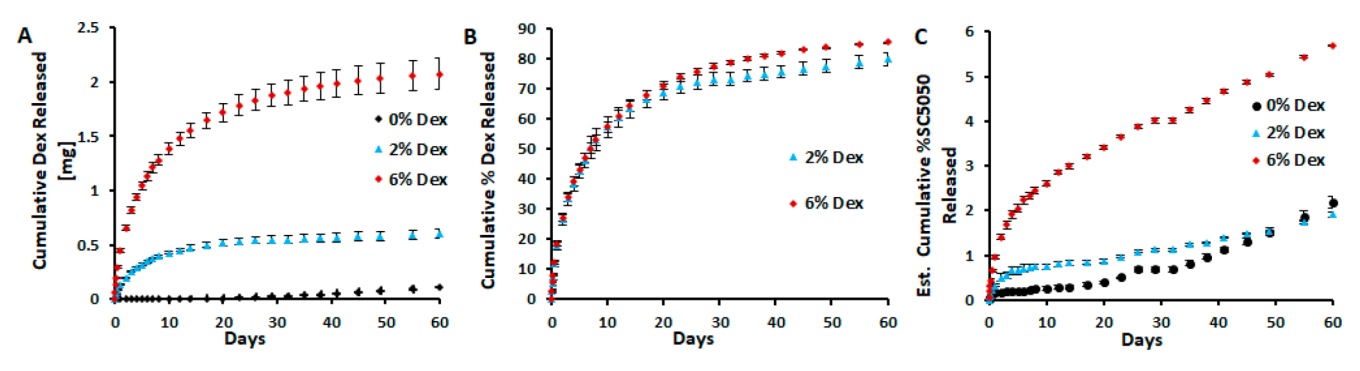
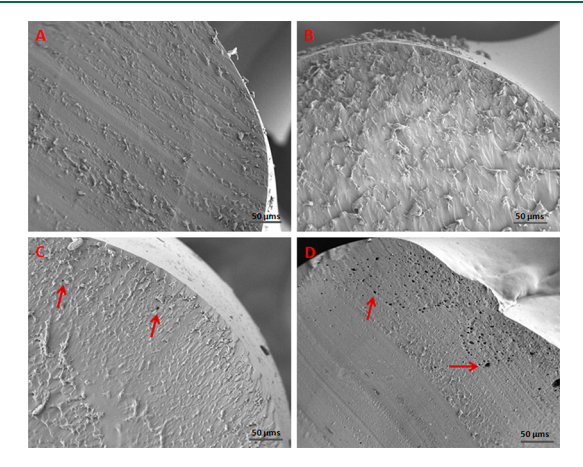


Figure 8. (A) Cumulative Dex released, (B) cumulative percent Dex (of initial loading) released, and (C) estimated cumulative percent SC5050 polyester released from the Dex-SC5050 3D printed scaffolds in vitro in PBS at 37 °C over 8 weeks.

1



**Figure 9.** SEM images of the cross section of the 3D printed scaffolds (A) before degradation and after in vitro degradation for the scaffolds with (B) 0%, (C) 2%, and (D) 6% w/w Dex in SC5050 polyesters.

increases the molecular mobility of the system, which can accelerate migration of Dex to the surface. Furthermore, the high porosity of the 3D printed scaffolds provides an inherently high surface area and, therefore, low migration distance from the bulk to the surface of the matrix. Thus, drug/polymer separation with surface connected drug domains, together with increased molecular mobility, high surface area, and the relatively higher solubility of Dex in water than in the SC5050 polyester, results in most of the drug being released in the initial few days as burst release.

The apparent biphasic release profiles shown in Figure 9A and B suggest a late-term slow release phase that is governed by diffusion of the drug molecules through the polymer matrix.<sup>76</sup> Once the surface-connected drug is released during the burst release phase, the drug release is driven by the diffusion and migration of drug molecules from within the matrix bulk to its surface. In the case of biodegradable polymers, this phase is generally accompanied by polymer hydrolysis and degradation.<sup>76</sup> Higher degradation rates of the polymer increase the rate of drug release due to more water penetration into the matrix. The influx of water leads to hydrolysis of the polyester chains, causing the matrix to swell and degrade, creating pores large enough for drug transport. This is generally a fast release phase, sometimes also referred to as the second burst release phase, and commonly observed in aliphatic polyesters like PLGA.<sup>76</sup> However, in the case of the SC5050 polyesters, the long fatty acid side chains make it relatively hydrophobic and reduce water permeability into the

matrix. Therefore, a second fast drug release phase is not observed for any of the Dex-SC5050 3D printed scaffolds.

**Polymer Degradation.** The SC5050 polyester undergoes degradation due to hydrolytic cleavage of the ester linkage along polymer backbone. Such hydrolytic degradation leads to random chain scission and reduction of polymer molecular weight. This removal of the cleaved chains from the polymer matrix is called erosion. We examined the change in erosion kinetics of the 3D printed polymer scaffolds, due to the presence of the loaded Dex, by analyzing the amount of the SC5050 polyester released in PBS at 37 °C over a period of 8 weeks. The amount of the SC5050 polyester released in the media was estimated based on the amount of the soybean (S) monomer in the collected solutions. Figure 8C shows the percent SC5050 polyester released from the Dex–SC5050 polyester 3D printed scaffolds.

Note that the 3D printed SC5050 polyester scaffolds without Dex degrade at a nearly constant rate. A linear regression analysis ( $R^2 = 0.93$ ) shows the degradation rate to be 15.8  $\mu$ g/day (see Figure S.8 in the Supporting Information). A linear degradation profile is generally a characteristic of surface eroding polymers. Hydrolytic surface erosion occurs when polymer degradation starts predominantly at the surface due to higher rate of erosion compared to the rate of water penetration in the bulk polymer. The size of the scaffold reduces uniformly from the exterior to the interior and, therefore, the overall shape of the scaffold is retained until most of the polymer degrades. Surface erosion kinetics is generally preferred in medical applications since it is controllable and reproducible. The surface of the scaffold is retained until most of the polymer degrades.

The presence of Dex in the 3D printed scaffold appears to induce a nonlinear polymer degradation profile. Dex loaded scaffolds degrade much faster than the SC5050 scaffolds without Dex over the first few days. Thus, the scaffolds with 2% and 6% w/w Dex in SC5050 polyester degrade at a rate of 66.3  $\mu$ g/day ( $R^2 = 0.93$ ) and 197.9  $\mu$ g/day ( $R^2 = 0.95$ ), respectively, over the first 3 days. After the initial surge in the degradation rate, the 2%, and 6% w/w Dex containing scaffolds degrade slower at a steady degradation rate of 7.9  $\mu$ g/day ( $R^2 = 0.98$ ) and 24.9  $\mu$ g/day ( $R^2 = 0.98$ ) (see Figure S.7 in the Supporting Information).

The surge in the amount of polymer released from Dex containing scaffolds coincides with the burst release of Dex, and this surge can be explained by rapid erosion of polymer surface potentially by the presence of pores created by the burst release of the drug from the surface of the polymer matrix. This is corroborated by higher degradation rate of the polymer from scaffolds with more Dex. The outward diffusion

of the drug creates water channels on the surface of the polymer matrix, which facilitates polymer surface erosion. Since the SC5050 polymer is very hydrophobic, water permeation into the bulk of a material is slow which results in lower rates of bulk polymer degradation. As expected, the scaffolds with higher drug compositions have higher rate of degradation since such scaffolds will have more pores formed by drug diffusion and higher surface area.

Figure 9 shows an SEM picture of the cross section of the 3D printed scaffolds, which sheds further light into the mechanism of erosion. Pores are observed in the cross section of the Dex loaded SC5050 polyester scaffolds after 8 weeks in vitro degradation in PBS at 37 °C

The pores are observed near the surface of the scaffold. The scaffolds with 6% w/w Dex have bigger and more numerous pores than the scaffolds with 2% w/w Dex. On the other hand, no pores were visible after degradation for the scaffold without Dex. The pores inside the polymer matrix are the regions that contained the drug particles before the drug is released. The presence of pores near the surface provides further evidence of phase separation of Dex from the polymer matrix and the presence of Dex near the surface of the polymer matrix.

In Vivo Evaluation of SC5050 Scaffolds. As a preliminary assessment of in vivo host response to the 3D printed SC5050 scaffolds, these scaffolds were implanted subcutaneously—caudally in Sprague—Dawley rats. After 6 weeks, the samples were retrieved (Figure 10A). Visually, no inflammation was visible during retrieval. The tissue surrounding the samples appeared redder, suggesting vascular

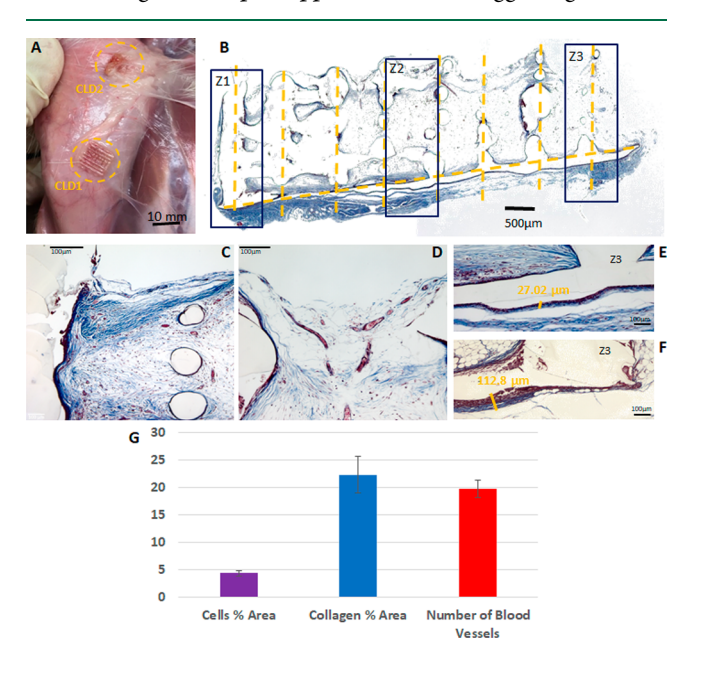


**Figure 10.** In vivo polymer biocompatibility evaluation. (a) Image of samples after 6-week implantation in a Sprague—Dawley rat. No sign of inflammation is visible, and the tissue around the samples had apparent vascularization. (b) Micrograph of a Masson's Trichrome stained section of a complete sample, showing the different zones (Z1, Z2, and Z3) where pictures were taken for analysis in ImageJ. (c, d) Micrographs of Masson Trichrome stained sections showing cell (purple, black) infiltration and collagen (blue) deposition in between the samples posts (clear). (e–f) Micrographs of Masson Trichrome stained sections showing minimal fibrous encapsulation at the bottom edge of the samples. (g) Quantitative analyses of blood vessels, cellular infiltration, and collagen deposition.

supply to the scaffolds was present. Qualitative assessment of the pictures of the sections stained with Masson's Trichrome showed minimal fibrous encapsulation around the polymer strands, with larger layers of collagen and cells present at the bottom edge of the samples. Cellular infiltration had reached the center of the graft for both groups. Blood vessels were also visible. Further quantitative analyses were performed using ImageJ (Figure 10G). The percentage of surface area covered by cells and collagen respectively was  $3.12 \pm 2.04\%$  and  $22.31 \pm 13.21\%$ . The analysis process is presented in the Supporting Information (Figure S.9). The number of blood vessels per image was also counted and averaged. An image highlighting the blood vessels in the tissue sample is shown in the SI (Figure S.10). Representative images are presented in Figure 10C-F. More images are presented in the SI (Figure S.11).

## CONCLUSION

3D printing can be used to create bioactive multicomponent scaffolds with desired performance properties. However, to create high quality 3D printed implants with desired performance, it is important to understand the interaction of a bioactive with a polymer and the impact the bioactive may have on polymer properties and its 3D printability.

In the case of a drug-polymer system, temperaturecomposition phase diagrams offer a framework to predict drug-polymer interaction and determine the maximum solubility and miscibility of the drug in the polymer. Based on the constructed Gibbs free energy and temperaturecomposition phase diagrams, we conclude that Dex is sparingly soluble ( $<2 \times 10^{-5}\%$  w/w) in SC5050 at the relevant 3D printing temperature. This conclusion was supported by rheology of the Dex-SC5050 mixtures, where the viscosity and shear modulus of the SC5050 polyester was higher when mixed with Dex, similar to the effect of immiscible fillers. Moreover, the presence of Dex led to higher shear thinning of the SC5050 polyester, as compared to Dex-free SC5050, when tested in steady state flow conditions. The shear thinning behavior is critical to extrusion-based 3D printing and can affect the printability of the material, as well as the quality of the 3D printed constructs.

The effect of composition of Dex on the quality of the 3D printed constructs was examined by individually analyzing the dimensions and shape of first six layers of 3D printed crosshatch scaffold. Increased line thickness was observed at the point of intersection of the crosshatch pattern due to the spreading of the deposited polymer over the previous layer until it is set by cross-linking. This spreading was reduced in the case of Dex loaded SC5050 polyester due to the increased viscosity of the mixture, which resulted in relatively more uniform filaments. The uniform filaments led to sharper corners at the intersection, increased pore area, and "higher quality" scaffolds. The quality or printability was evaluated by measuring deviation in the pore shape from expected rectangular shape. The printability of the first two layers was different than the rest of the layers of the scaffold. This is because the first layer is deposited on a different substrate, usually glass, which affects the printability of the first layer and a few following layers. The drug release and polymer degradation kinetics from the 3D printed scaffolds was analyzed in vitro in PBS at 37  $^{\circ}\text{C}$  over 8 weeks. A burst release of Dex was observed, with more than 50% of the loaded drug being released in the first 10 days. The burst release kinetics suggests most of the drug is present near the surface of the 3D printed matrix. This is confirmed by SEM of the scaffold cross section where pores, formed due to dissolution of the drug, were observed near the surface of the 3D printed matrix. The presence of the drug also affects the polymer degradation kinetics and erosion mechanism. Accelerated degradation was observed initially in case of the Dex loaded SC5050 3D printed scaffolds.

The preliminary biocompatibility of the SC5050 3D printed scaffolds was assessed by implanting them in vivo in rats for 6 weeks. Cell infiltration was observed through the center of the scaffolds. Collagen was found mainly near the bottom of the scaffolds. Blood vessels were also observed. The current results point to the utility of the SC5050 scaffolds for tissue engineering applications.

To develop a universal understanding on the effect of bioactive fillers on the printability and quality of 3D printed constructs, we plan to investigate the effect of other drugs on the 3D printing of the SC5050 polyesters. Further understanding of how the composition of different bioactive fillers can affect the 3D printing quality and scaffold performance, and how 3D printing may impact the potency of incorporated bioactive fillers, is crucial for facilitating the development of personalized bioactive medical implants for tissue engineering applications.

## ASSOCIATED CONTENT

# **S** Supporting Information

The Supporting Information is available free of charge on the ACS Publications website at DOI: 10.1021/acsbiomaterials.8b00964.

Data used for supporting the observations in this article (Figure S1-S9) (PDF)

## AUTHOR INFORMATION

#### **Corresponding Authors**

\*Email: abraham@uakron.edu (A.J.).
\*Email: irada.isayeva@fda.hhs.gov (I.I.).

ORCID ®

Abraham Joy: 0000-0001-7781-3817

# **Author Contributions**

T.J. and Q.L. synthesized the polymers. C.P. and J.F. designed, performed, and analyzed the in vivo experiments. V.P. and R.K. recorded the UV—vis spectroscopy data. D.S. analyzed and modeled the UV—vis spectroscopy data. T.J., D.S, J.C., A.J., and I.I. designed the experiments and wrote the manuscript.

#### Funding

The work described herein was funded by NSF/FDA SIR grants (NSF DMR 1641081 and 1542065).

#### Notes

The authors declare no competing financial interest.

### ACKNOWLEDGMENTS

The authors would like to acknowledge Dr. Srilekha Das, Dr. Centeno Jose, and Dr. Samanthi Wickramasekara for the valuable discussions.

## REFERENCES

- (1) Murphy, S. V.; Atala, A. 3D bioprinting of tissues and organs. *Nat. Biotechnol.* **2014**, 32 (8), 773–85.
- (2) Gross, B. C.; Erkal, J. L.; Lockwood, S. Y.; Chen, C.; Spence, D. M. Evaluation of 3D printing and its potential impact on

- biotechnology and the chemical sciences. Anal. Chem. 2014, 86 (7), 3240-53.
- (3) Ventola, C. L. Medical applications for 3D printing: current and projected uses. *P* & *T* **2014**, 39 (10), 704.
- (4) Billiet, T.; Vandenhaute, M.; Schelfhout, J.; Van Vlierberghe, S.; Dubruel, P. A review of trends and limitations in hydrogel-rapid prototyping for tissue engineering. *Biomaterials* **2012**, 33 (26), 6020–41
- (5) Chia, H. N.; Wu, B. M. Recent advances in 3D printing of biomaterials. J. Biol. Eng. 2015, 9, 4.
- (6) Pati, F.; Gantelius, J.; Svahn, H. A. 3D Bioprinting of Tissue/Organ Models. *Angew. Chem., Int. Ed.* **2016**, 55 (15), 4650–65.
- (7) Kim, B. J.; Hong, K. S.; Park, K. J.; Park, D. H.; Chung, Y. G.; Kang, S. H. Customized cranioplasty implants using three-dimensional printers and polymethyl-methacrylate casting. *J. Korean Neurosurg. Soc.* **2012**, *52* (6), 541–6.
- (8) Gerber, N.; Stieglitz, L.; Peterhans, M.; Nolte, L. P.; Raabe, A.; Weber, S. Using rapid prototyping molds to create patient specific polymethylmethacrylate implants in cranioplasty. *Conf Proc. IEEE Eng. Med. Biol. Soc.* **2010**, 3357–60.
- (9) Parthasarathy, J. 3D modeling, custom implants and its future perspectives in craniofacial surgery. *Ann. Maxillofac Surg* **2014**, *4* (1), 9–18.
- (10) Chang, C. C.; Boland, E. D.; Williams, S. K.; Hoying, J. B. Direct-write bioprinting three-dimensional biohybrid systems for future regenerative therapies. *J. Biomed. Mater. Res., Part B* **2011**, 98 (1), 160–70.
- (11) Karageorgiou, V.; Kaplan, D. Porosity of 3D biomaterial scaffolds and osteogenesis. *Biomaterials* **2005**, *26* (27), 5474–91.
- (12) Fedorovich, N. E.; Alblas, J.; Hennink, W. E.; Oner, F. C.; Dhert, W. J. Organ printing: the future of bone regeneration? *Trends Biotechnol.* **2011**, 29 (12), 601–6.
- (13) Balakrishnan, B.; Banerjee, R. Biopolymer-based hydrogels for cartilage tissue engineering. *Chem. Rev.* **2011**, *111* (8), 4453–74.
- (14) Jungst, T.; Smolan, W.; Schacht, K.; Scheibel, T.; Groll, J. Strategies and Molecular Design Criteria for 3D Printable Hydrogels. *Chem. Rev.* **2016**, *116* (3), 1496–539.
- (15) Bertassoni, L. E.; Cardoso, J. C.; Manoharan, V.; Cristino, A. L.; Bhise, N. S.; Araujo, W. A.; Zorlutuna, P.; Vrana, N. E.; Ghaemmaghami, A. M.; Dokmeci, M. R.; Khademhosseini, A. Direct-write bioprinting of cell-laden methacrylated gelatin hydrogels. *Biofabrication* **2014**, *6* (2), 024105.
- (16) Luo, Y.; Lode, A.; Wu, C.; Chang, J.; Gelinsky, M. Alginate/nanohydroxyapatite scaffolds with designed core/shell structures fabricated by 3D plotting and in situ mineralization for bone tissue engineering. ACS Appl. Mater. Interfaces 2015, 7 (12), 6541–9.
- (17) Hutmacher, D. W. Scaffolds in tissue engineering bone and cartilage. *Biomaterials* **2000**, *21* (24), 2529–43.
- (18) Yang, G. H.; Kim, M.; Kim, G. Additive-manufactured polycaprolactone scaffold consisting of innovatively designed microsized spiral struts for hard tissue regeneration. *Biofabrication* **2017**, 9 (1), 015005.
- (19) Shim, J. H.; Kim, S. E.; Park, J. Y.; Kundu, J.; Kim, S. W.; Kang, S. S.; Cho, D. W. Three-dimensional printing of rhBMP-2-loaded scaffolds with long-term delivery for enhanced bone regeneration in a rabbit diaphyseal defect. *Tissue Eng., Part A* **2014**, *20* (13–14), 1980–92.
- (20) Lin, Z. Y.; Duan, Z. X.; Guo, X. D.; Li, J. F.; Lu, H. W.; Zheng, Q. X.; Quan, D. P.; Yang, S. H. Bone induction by biomimetic PLGA-(PEG-ASP)n copolymer loaded with a novel synthetic BMP-2-related peptide in vitro and in vivo. *J. Controlled Release* **2010**, *144* (2), 190–5
- (21) Ma, R.; Tang, T. Current strategies to improve the bioactivity of PEEK. Int. J. Mol. Sci. 2014, 15 (4), 5426-45.
- (22) Sun, L.; Parker, S. T.; Syoji, D.; Wang, X.; Lewis, J. A.; Kaplan, D. L. Direct-write assembly of 3D silk/hydroxyapatite scaffolds for bone co-cultures. *Adv. Healthcare Mater.* **2012**, *1* (6), 729–35.

- (23) Michna, S.; Wu, W.; Lewis, J. A. Concentrated hydroxyapatite inks for direct-write assembly of 3-D periodic scaffolds. *Biomaterials* **2005**, 26 (28), 5632–9.
- (24) Ang, T. H.; Sultana, F. S. A.; Hutmacher, D. W.; Wong, Y. S.; Fuh, J. Y. H.; Mo, X. M.; Loh, H. T.; Burdet, E.; Teoh, S. H. Fabrication of 3D Chitosan Hydroxyapatite Scaffolds Using a Robotic Dispensing Arm. *Mater. Sci. Eng., C* **2002**, *20*, 35–42.
- (25) Amini, A. R.; Laurencin, C. T.; Nukavarapu, S. P. Nukavarapu, Bone Tissue Engineering Recent Advances and Challenges. *Crit Rev. Biomed Eng.* **2012**, *40* (5), 363–408.
- (26) Henkel, J.; Woodruff, M. A.; Epari, D. R.; Steck, R.; Glatt, V.; Dickinson, I. C.; Choong, P. F.; Schuetz, M. A.; Hutmacher, D. W. Bone Regeneration Based on Tissue Engineering Conceptions A 21st Century Perspective. *Bone Res.* 2013, 1 (3), 216–48.
- (27) Wu, C.; Luo, Y.; Cuniberti, G.; Xiao, Y.; Gelinsky, M. Three-dimensional printing of hierarchical and tough mesoporous bioactive glass scaffolds with a controllable pore architecture, excellent mechanical strength and mineralization ability. *Acta Biomater.* **2011**, 7 (6), 2644–50.
- (28) Prestwich, G. D. Hyaluronic acid-based clinical biomaterials derived for cell and molecule delivery in regenerative medicine. *J. Controlled Release* **2011**, *155* (2), 193–9.
- (29) Yu, D. G.; Shen, X. X.; Branford-White, C.; Zhu, L. M.; White, K.; Yang, X. L. Novel oral fast-disintegrating drug delivery devices with predefined inner structure fabricated by Three-Dimensional Printing. *J. Pharm. Pharmacol.* **2009**, *61* (3), 323–9.
- (30) Lee, B. K.; Yun, Y. H.; Choi, J. S.; Choi, Y. C.; Kim, J. D.; Cho, Y. W. Fabrication of drug-loaded polymer microparticles with arbitrary geometries using a piezoelectric inkjet printing system. *Int. J. Pharm.* **2012**, 427 (2), 305–10.
- (31) Gbureck, U.; Vorndran, E.; Muller, F. A.; Barralet, J. E. Low temperature direct 3D printed bioceramics and biocomposites as drug release matrices. *J. Controlled Release* **2007**, *122* (2), 173–80.
- (32) Scoutaris, N.; Alexander, M. R.; Gellert, P. R.; Roberts, C. J. Inkjet printing as a novel medicine formulation technique. *J. Controlled Release* **2011**, *156* (2), 179–85.
- (33) Pardeike, J.; Strohmeier, D. M.; Schrodl, N.; Voura, C.; Gruber, M.; Khinast, J. G.; Zimmer, A. Nanosuspensions as advanced printing ink for accurate dosing of poorly soluble drugs in personalized medicines. *Int. J. Pharm.* **2011**, 420 (1), 93–100.
- (34) Shenoy, A. V. Rheology of Filled Polymer Systems 1999, 1.
- (35) Filled Elastomers Drug Delivery Systems; Springer-Verlag: Berlin Heidelberg, 2002.
- (36) Compton, B. G.; Lewis, J. A. 3D-printing of lightweight cellular composites. *Adv. Mater.* **2014**, 26 (34), 5930–5.
- (37) Hwang, S.; Reyes, E. I.; Moon, K.-s.; Rumpf, R. C.; Kim, N. S. Thermo-mechanical Characterization of Metal/Polymer Composite Filaments and Printing Parameter Study for Fused Deposition Modeling in the 3D Printing Process. *J. Electron. Mater.* **2015**, 44 (3), 771–777.
- (38) Aho, J.; Edinger, M.; Botker, J.; Baldursdottir, S.; Rantanen, J. Oscillatory Shear Rheology in Examining the Drug-Polymer Interactions Relevant in Hot Melt Extrusion. *J. Pharm. Sci.* **2016**, 105 (1), 160–7.
- (39) Sarode, A. L.; Sandhu, H.; Shah, N.; Malick, W.; Zia, H. Hot melt extrusion (HME) for amorphous solid dispersions: predictive tools for processing and impact of drug-polymer interactions on supersaturation. *Eur. J. Pharm. Sci.* **2013**, *48* (3), 371–84.
- (40) Genina, N.; Hollander, J.; Jukarainen, H.; Makila, E.; Salonen, J.; Sandler, N. Ethylene vinyl acetate (EVA) as a new drug carrier for 3D printed medical drug delivery devices. *Eur. J. Pharm. Sci.* **2016**, *90*, 53–63.
- (41) Goyanes, A.; Buanz, A. B.; Basit, A. W.; Gaisford, S. Fused-filament 3D printing (3DP) for fabrication of tablets. *Int. J. Pharm.* **2014**, 476 (1–2), 88–92.
- (42) Goyanes, A.; Det-Amornrat, U.; Wang, J.; Basit, A. W.; Gaisford, S. 3D scanning and 3D printing as innovative technologies for fabricating personalized topical drug delivery systems. *J. Controlled Release* **2016**, 234, 41–8.

- (43) Goyanes, A.; Kobayashi, M.; Martinez-Pacheco, R.; Gaisford, S.; Basit, A. W. Fused-filament 3D printing of drug products: Microstructure analysis and drug release characteristics of PVA-based caplets. *Int. J. Pharm.* **2016**, *514* (1), 290–295.
- (44) Melocchi, A.; Parietti, F.; Loreti, G.; Maroni, A.; Gazzaniga, A.; Zema, L. 3D printing by fused deposition modeling (FDM) of a swellable/erodible capsular device for oral pulsatile release of drugs. *J. Drug Delivery Sci. Technol.* **2015**, *30*, 360–367.
- (45) Melocchi, A.; Parietti, F.; Maroni, A.; Foppoli, A.; Gazzaniga, A.; Zema, L. Hot-melt extruded filaments based on pharmaceutical grade polymers for 3D printing by fused deposition modeling. *Int. J. Pharm.* **2016**, 509 (1–2), 255–263.
- (46) Sadia, M.; Sosnicka, A.; Arafat, B.; Isreb, A.; Ahmed, W.; Kelarakis, A.; Alhnan, M. A. Adaptation of pharmaceutical excipients to FDM 3D printing for the fabrication of patient-tailored immediate release tablets. *Int. J. Pharm.* **2016**, *513* (1–2), 659–668.
- (47) Marsac, P. J.; Rumondor, A. C.; Nivens, D. E.; Kestur, U. S.; Stanciu, L.; Taylor, L. S. Effect of temperature and moisture on the miscibility of amorphous dispersions of felodipine and poly(vinyl pyrrolidone). *J. Pharm. Sci.* **2010**, *99* (1), 169–85.
- (48) Chokshi, R. J.; Sandhu, H. K.; Iyer, R. M.; Shah, N. H.; Malick, A. W.; Zia, H. Characterization of physico-mechanical properties of indomethacin and polymers to assess their suitability for hot-melt extrusion processs as a means to manufacture solid dispersion/solution. *J. Pharm. Sci.* 2005, 94 (11), 2463–74.
- (49) Govindarajan, S. R.; Xu, Y.; Swanson, J. P.; Jain, T.; Lu, Y.; Choi, J.-W.; Joy, A. A Solvent and Initiator Free, Low-Modulus, Degradable Polyester Platform with Modular Functionality for Ambient-Temperature 3D Printing. *Macromolecules* **2016**, 49 (7), 2429–2437.
- (50) Tian, Y.; Booth, J.; Meehan, E.; Jones, D. S.; Li, S.; Andrews, G. P. Construction of drug-polymer thermodynamic phase diagrams using Flory-Huggins interaction theory: identifying the relevance of temperature and drug weight fraction to phase separation within solid dispersions. *Mol. Pharmaceutics* **2013**, *10* (1), 236–48.
- (51) Zhao, Y.; Inbar, P.; Chokshi, H. P.; Malick, A. W.; Choi, D. S. Prediction of the thermal phase diagram of amorphous solid dispersions by Flory-Huggins theory. *J. Pharm. Sci.* **2011**, *100* (8), 3196–207.
- (52) Donnelly, C.; Tian, Y.; Potter, C.; Jones, D. S.; Andrews, G. P. Probing the effects of experimental conditions on the character of drug-polymer phase diagrams constructed using Flory-Huggins theory. *Pharm. Res.* **2015**, 32 (1), 167–79.
- (53) Bansal, K.; Baghel, U. S.; Thakral, S. Construction and Validation of Binary Phase Diagram for Amorphous Solid Dispersion Using Flory-Huggins Theory. *AAPS PharmSciTech* **2016**, *17* (2), 318–27.
- (54) Huang, Y.; Dai, W. G. Fundamental aspects of solid dispersion technology for poorly soluble drugs. *Acta Pharm. Sin. B* **2014**, *4* (1), 18–25.
- (55) Knopp, M. M.; Tajber, L.; Tian, Y.; Olesen, N. E.; Jones, D. S.; Kozyra, A.; Lobmann, K.; Paluch, K.; Brennan, C. M.; Holm, R.; Healy, A. M.; Andrews, G. P.; Rades, T. Comparative Study of Different Methods for the Prediction of Drug-Polymer Solubility. *Mol. Pharmaceutics* **2015**, *12* (9), 3408–19.
- (56) Thakral, S.; Thakral, N. K. Prediction of drug—polymer miscibility through the use of solubility parameter based Flory-Huggins interaction parameter and the experimental validation: PEG as model polymer. J. Pharm. Sci. 2013, 102 (7), 2254–63.
- (57) Siegel, S. J.; Kahn, J. B.; Metzger, K.; Winey, K. I.; Werner, K.; Dan, N. Effect of drug type on the degradation rate of PLGA matrices. *Eur. J. Pharm. Biopharm.* **2006**, 64 (3), 287–93.
- (58) D'Souza, S.; Faraj, J. A.; Dorati, R.; DeLuca, P. P. Enhanced Degradation of Lactide-co-Glycolide Polymer with Basic Nucleophilic Drugs. *Advances in Pharmaceutics* **2015**, 2015, 1–10.
- (59) Gomez-Gaete, C.; Tsapis, N.; Besnard, M.; Bochot, A.; Fattal, E. Encapsulation of dexamethasone into biodegradable polymeric nanoparticles. *Int. J. Pharm.* **2007**, *331* (2), 153–9.

- (60) Leuner, C. Improving Drug Solubility for Oral Delivery Using Solid Dispersions. *Eur. J. Pharm. Biopharm.* **2000**, *50*, 47–60.
- (61) Marsac, P. J.; Li, T.; Taylor, L. S. Estimation of drug—polymer miscibility and solubility in amorphous solid dispersions using experimentally determined interaction parameters. *Pharm. Res.* **2009**, 26 (1), 139–51.
- (62) Paudel, A.; et al. Theoretical and Experimental Investigation on the Solid Solubility and Miscibility of Naproxen in PVP. *Mol. Pharmaceutics* **2010**, *7* (4), 1133–1148.
- (63) Lin, D.; Huang, Y. A thermal analysis method to predict the complete phase diagram of drug-polymer solid dispersions. *Int. J. Pharm.* **2010**, 399 (1–2), 109–15.
- (64) Guo, T.; Holzberg, T. R.; Lim, C. G.; Gao, F.; Gargava, A.; Trachtenberg, J. E.; Mikos, A. G.; Fisher, J. P. 3D printing PLGA: a quantitative examination of the effects of polymer composition and printing parameters on print resolution. *Biofabrication* **2017**, *9* (2), 024101
- (65) Li, Y.; Pang, H.; Guo, Z.; Lin, L.; Dong, Y.; Li, G.; Lu, M.; Wu, C. Interactions between drugs and polymers influencing hot melt extrusion. *J. Pharm. Pharmacol.* **2014**, *66* (2), 148–66.
- (66) Van Renterghem, J.; Vervaet, C.; De Beer, T. Rheological Characterization of Molten Polymer-Drug Dispersions as a Predictive Tool for Pharmaceutical Hot-Melt Extrusion Processability. *Pharm. Res.* **2017**, *34* (11), 2312–2321.
- (67) Aho, J.; Boetker, J. P.; Baldursdottir, S.; Rantanen, J. Rheology as a tool for evaluation of melt processability of innovative dosage forms. *Int. J. Pharm.* **2015**, 494 (2), 623–42.
- (68) Maru, S. M.; de Matas, M.; Kelly, A.; Paradkar, A. Characterization of thermal and rheological properties of zidovudine, lamivudine and plasticizer blends with ethyl cellulose to assess their suitability for hot melt extrusion. *Eur. J. Pharm. Sci.* **2011**, *44* (4), 471–8.
- (69) Suwardie, H.; Wang, P.; Todd, D. B.; Panchal, V.; Yang, M.; Gogos, C. G. Rheological study of the mixture of acetaminophen and polyethylene oxide for hot-melt extrusion application. *Eur. J. Pharm. Biopharm.* **2011**, 78 (3), 506–12.
- (70) Bailly, M.; Kontopoulou, M.; El Mabrouk, K. Effect of polymer/filler interactions on the structure and rheological properties of ethylene-octene copolymer/nanosilica composites. *Polymer* **2010**, *51* (23), 5506–5515.
- (71) White, J. L.; Crowder, J. W. The Influence of Carbon Black on The Extrusion Characteristics and Rheological Properties of Elastomers. *J. Appl. Polym. Sci.* **1974**, *18*, 1013–1038.
- (72) Stamhuis, J. E.; Lopp, J. P. A. Rheological Determination of Polymer-Filler Affinity. *Rheol. Acta* 1982, 21, 103–105.
- (73) Minagawa, N.; White, J. L. The Influence of Titanium Dioxide on the Rheological and Extrusion Properties of Polymer Melts. *J. Appl. Polym. Sci.* **1976**, 20, 501–523.
- (74) Vlachopoulos, D. S. The Role of Rheology in Polymer Extrusion. In Extrusion Minitec and Conference: From Basics to Recent Developments, 2003.
- (75) Ouyang, L.; Yao, R.; Zhao, Y.; Sun, W. Effect of bioink properties on printability and cell viability for 3D bioplotting of embryonic stem cells. *Biofabrication* **2016**, *8* (3), 035020.
- (76) Kamaly, N.; Yameen, B.; Wu, J.; Farokhzad, O. C. Degradable Controlled-Release Polymers and Polymeric Nanoparticles: Mechanisms of Controlling Drug Release. *Chem. Rev.* **2016**, *116* (4), 2602–63.
- (77) Fu, Y.; Kao, W. J. Drug release kinetics and transport mechanisms of non-degradable and degradable polymeric delivery systems. *Expert Opin. Drug Delivery* **2010**, 7 (4), 429–44.
- (78) Vo, C. L.; Park, C.; Lee, B. J. Current trends and future perspectives of solid dispersions containing poorly water-soluble drugs. Eur. J. Pharm. Biopharm. 2013, 85, 799–813.
- (79) Burkersroda, F. v.; et al. Why Degradable Polymers Undergo Surface Erosion or Bulk Erosion. *Biomaterials* **2002**, 23, 4221–4231.